




**Nuclear spectra from low-energy interactions**J. Ljungberg, B. G. Carlsson, J. Rotureau , A. Idini , and I. Ragnarsson *Mathematical Physics, LTH, Lund University, S-22100 Lund, Sweden*

(Received 22 April 2022; accepted 7 July 2022; published 25 July 2022)

A method to describe spectra starting from nuclear density functionals is explored. The idea is based on postulating an effective Hamiltonian that reproduces the stiffness associated with collective modes. The method defines a simple form of such an effective Hamiltonian and a mapping to go from a density functional to the corresponding Hamiltonian. In order to test the method, the Hamiltonian is constrained using a Skyrme functional and solved with the generator-coordinate method to describe low-lying levels and electromagnetic transitions in  $^{48,49,50,52}\text{Cr}$  and  $^{24}\text{Mg}$ .

DOI: [10.1103/PhysRevC.106.014314](https://doi.org/10.1103/PhysRevC.106.014314)**I. INTRODUCTION**

A starting point for the description of nuclei is the assumption that low-energy properties can be described using a combination of two- and three-body interactions. This sought after Hamiltonian should be applicable to all nuclei and give reliable predictions for properties that are not yet measured. A possible route for finding such an interaction comes from Skyrme's expansion in the relative momenta of interacting nucleons [1]. This expansion can be carried out to higher orders [2,3] and recently the first applications of such higher-order interactions has emerged [4].

For essentially all applications, such as descriptions of fission and for systematic descriptions of nuclei and reactions, the method has to be numerically efficient in order to be useful. This leads to approximations where, for example, finite-range three-body interactions can not be treated explicitly and the three-body part is conveniently described as a density-dependent two-body interaction. The resulting approximations are known as nuclear energy density functionals [5] (EDFs). When used in connection with Hartree-Fock-Bogoliubov (HFB) approximations they describe ground-state masses with an error of around 0.7 MeV [6]. When used in other approaches such as the quasiparticle-random-phase approximation (QRPA) they describe many observables such as low-lying excitations and strength functions [7,8]. This indicates that the original assumption of a common low-energy interaction applicable to all nuclei is not that far fetched.

Nuclei have a tendency towards spontaneous symmetry breaking, in particular pertaining to their shapes. Therefore, in order to capture physical effects the description with EDFs

is based on the breaking of symmetries. This leads to intuitive and rather accurate descriptions in terms of deformed nuclei with broken quantum numbers. However, in an exact treatment, the nuclear wave functions should be eigenstates of operators corresponding to conserved quantities, such as the squared total angular momentum operator. Methods that restore the symmetries give corrections to binding energies and allow a direct comparison of observables, such as energy levels, to experiment. Restoration of symmetries can be done in several ways but a common theme is to reduce the degrees of freedom of the system in order to keep the efficiency and applicability of the methods.

Several such approaches have been developed that do not introduce any free parameters but rather determine the parameters from the response of the EDFs to external fields. Examples of such approaches include; the particle(s)-rotor model [9], where the system is divided into a collective rotor part and a particle part; the Bohr Hamiltonian, where also vibrations of the shape of the rotor are included [10]; the interacting boson-fermion model [11], where the degrees of freedom are mapped into interacting effective particles; as well as methods to construct effective simpler Hamiltonians from underlying EDFs [12].

One of the most promising directions for symmetry restoration is based on the generating coordinate method (GCM) where the problem of choosing degrees of freedom is converted into choosing an appropriate subspace of nonorthogonal many-body basis states. The degrees of freedom are instead selected by choosing external fields for sampling of the space. Its microscopic nature and the possibilities for systematic convergence are part of the appealing features of the GCM. In principle it can be applied using a full low-energy interaction with finite range two- and three-body terms. However, to construct an efficient and applicable approach it would be very convenient to be able to apply it together with the already developed EDFs.

In this respect, one issue is that models for the low-momentum part of the interaction also contain a high-momentum part that may not give physical results if it is

---

*Published by the American Physical Society under the terms of the [Creative Commons Attribution 4.0 International](https://creativecommons.org/licenses/by/4.0/) license. Further distribution of this work must maintain attribution to the author(s) and the published article's title, journal citation, and DOI. Funded by Bibsam.*

not constrained. In Hartree-Fock type of calculations, the high-momentum part of the interaction is never probed. However, extensions that attempt to sum up correlation energies may require momentum cutoffs in order to avoid ultraviolet divergencies [13]. A second issue is how to treat the density-dependent part of the interaction. There are various approaches for obtaining approximate matrix elements between many-body states that should represent the physics contained in the density-dependent part of the interaction. However, a difficulty in finding consistent approaches is that approximations that violate the Pauli principle lead to poles that can cause nonphysical contributions to the energy [14,15].

In this paper we use a Skyrme-based EDF to constrain a simple effective Hamiltonian that is based on the fundamental nuclear degrees of freedom of quadrupole deformation and pairing. The Hamiltonian may be considered to be composed of the first terms in a series where degrees of freedom are chosen through the selected multipole operators and the precision of the expansion is determined by the number of terms included. This Hamiltonian is used in GCM calculations, restoring the broken symmetries, to obtain the ground-state binding energies, nuclear spectra, and transitions for even and odd nuclei. We take particular care to include all exchange terms in order to avoid any spurious pole contributions and make use of recent developments in the calculation of overlaps of Bogoliubov states [16]. We recently applied the same approach to describe excitations in superheavy nuclei [17]. Here we provide a more detailed description of the formalism and present results for several lighter nuclei, including electromagnetic transition probabilities.

In Sec. II we detail the structure of the Hamiltonian and the procedure to link it to the EDF. In sec III we apply the method to several nuclei and compare spectra and transitions with experiment. In Sec. IV we summarize our conclusions from the study. Further details on the many-body formalism are given in the Appendix.

## II. MODEL

### A. Effective Hamiltonian

The starting point is the definition of an effective Hamiltonian. This will eventually be solved in a basis of HFB states using the GCM approach. In order to have an efficient and applicable method, the Hamiltonian is chosen as:

$$\hat{H} = \hat{H}_0 + \hat{H}_Q + \hat{H}_P. \quad (1)$$

$H$  includes three components to capture the most important physical effects: a spherical single-particle (SP) potential  $H_0$  that averages the interaction among nucleus, a quadrupole-quadrupole interaction  $H_Q$  that takes into account the quadrupole deformation, and finally, a pairing term  $H_P$  to consider neutron-neutron and proton-proton pairing correlations.

The SP potential is written as

$$\hat{H}_0 = \sum_i e_i a_i^\dagger a_i + E_0, \quad (2)$$

where  $i \equiv (q_i n_i l_i j_i m_i)$  denotes an orbital in a spherical basis labeled with its particle species  $q_i$  ( $=p$  or  $n$ ), principal

quantum number  $n_i$ , angular momentum  $l_i$ , total angular momentum  $j_i$ , and its projection  $m_i$ . The  $e_i$  are the single-particle energies and  $E_0$  is a constant. For convenience, a separable form is chosen for both  $\hat{H}_Q$  and  $\hat{H}_P$ .

The quadrupole-quadrupole separable interaction is given by

$$\hat{H}_Q = -\frac{1}{4}\chi \sum_{ijkl} \sum_{\mu} [\tilde{Q}_{ik}^{2\mu} \tilde{Q}_{lj}^{2\mu*} - \tilde{Q}_{il}^{2\mu} \tilde{Q}_{kj}^{2\mu*}] a_i^\dagger a_j^\dagger a_l a_k, \quad (3)$$

where  $\chi$  is the interaction strength and  $\tilde{Q}_{ij}^{2\mu}$  are the matrix elements of a modified quadrupole operator with a radial form factor. In this case, the form factor is based on a Woods-Saxon potential from [18] (cf. Sec. II B).

For the pairing part we adopt the seniority pairing interaction [19]

$$\hat{H}_P = -\frac{1}{4} \sum_{ijkl} G_{ik} P_{ij} P_{kl} a_i^\dagger a_j^\dagger a_l a_k, \quad (4)$$

where  $G_{ik} = G_p \delta_{q_i, p} \delta_{q_k, p} + G_n \delta_{q_i, n} \delta_{q_k, n}$  is the pairing strength and

$$P_{ij} = (-1)^{j_i - m_i} \delta_{(qnlj)_i, (qnlj)_j} \delta_{m_i, -m_j}, \quad (5)$$

indicates the coupling of time-reversal pairs only. The seniority pairing is the simplest form of pairing interaction, which nonetheless enables a quantitative account of pairing phenomena and many-body correlations [20–22]. We fix the pairing strength  $G$  according to the uniform spectra method [19] (see Sec. II B).

The resulting Hamiltonian contains the monopole, pairing, and quadrupole components. These are the well known dominant contributions responsible, e.g., for the behavior of isotopic chains and the shell evolution until the drip lines [23]. The Hamiltonian preserves symmetries, such as exchange, rotational invariance, and parity. Isospin is violated by the quadrupole interaction that has a Coulomb part in the form factor. The translational symmetry is also broken both by the introduction of a single-particle potential, and by the decomposition of the interaction into a finite number of separable terms. This is, however, the case with any interaction represented on a grid of basis functions.

### B. Determination of coupling constants

The  $H_0$  part of the Hamiltonian is taken as the spherical Hartree-Fock (HF) potential from a Skyrme functional that will be the reference for the effective Hamiltonian. The constant  $E_0$  is taken to reproduce the corresponding spherical HF binding energy. The quadrupole part is also constructed to agree with the Skyrme results.

For neutrons, the quadrupole operator in  $\hat{H}_Q$  is taken from the modified quadrupole force in Ref. [18],

$$\tilde{Q}_{ij}^{2\mu} = \langle i | \tilde{Q}_p^{2\mu} | j \rangle \delta_{q_i, p} \delta_{q_j, p} + \langle i | \tilde{Q}_n^{2\mu} | j \rangle \delta_{q_i, n} \delta_{q_j, n}, \quad (6)$$

where

$$\tilde{Q}_n^{2\mu} = Y_{2\mu} \left( -R_n W_n \frac{\partial f_n(r)}{\partial r} + \frac{W_n v_{so} \lambda^2}{2} \frac{\partial^2 f_n(r)}{\partial r^2} \vec{l} \cdot \vec{s} \right), \quad (7)$$

TABLE I. Parameters defining the quadrupole interaction. For  $W$  the upper sign is associated with protons and lower sign with neutrons.

Quantity	Definition
$R_q$	$= 0.9\sqrt{\frac{5}{3}\langle r^2 \rangle_q}$
$a$	$= 0.9$ fm
$W^{p/n}$	$= V_0(1 \pm \kappa \frac{N-Z}{N+Z})$
$V_0$	$= -49.6$ MeV
$\kappa$	$= 0.86$
$v_{s.o.}$	$= 32$ (MeV s) $^{-2}$
$\lambda$	$= \frac{\hbar}{Mc}(1 + A^{-1})$
$M$	$= 939$ MeV/ $c^2$

and

$$f_n(r) = \frac{1}{1 + e^{(r-R_n)/a}}. \quad (8)$$

The proton part of the quadrupole operator

$$\begin{aligned} \hat{Q}_p^{2\mu} = & Y_{2\mu} \left( -r \frac{\partial H_c}{\partial r} \right. \\ & \left. - R_p W_p \frac{\partial f_p(r)}{\partial r} + \frac{W_p v_{s.o.} \lambda^2}{2} \frac{\partial^2 f_p(r)}{\partial r^2} \vec{l} \cdot \vec{s} \right), \end{aligned} \quad (9)$$

$$- R_p W_p \frac{\partial f_p(r)}{\partial r} + \frac{W_p v_{s.o.} \lambda^2}{2} \frac{\partial^2 f_p(r)}{\partial r^2} \vec{l} \cdot \vec{s}), \quad (10)$$

has an additional dependence on the Coulomb potential

$$H_c = \frac{Ze^2}{4\pi\epsilon_0} \left( \frac{1}{r} \theta(r - R_p) + \frac{1}{R_p} \left( \frac{3}{2} - \frac{1}{2} \left( \frac{r}{R_p} \right)^2 \theta(R_p - r) \right) \right). \quad (11)$$

The quadrupole operators depend on the two radius parameters  $R_p$  and  $R_n$  for the proton and neutron densities. These are determined from the expectation value of  $r^2$  calculated from the spherical Hartree-Fock solutions of the reference functional.

All the parameters of the interaction are in Table I. We keep the spin-orbit strength of [18] but we use universal parametrization [24] for the other values. The diffuseness constant is taken to be larger than in Ref. [24] since in our initial tests we found that a larger value generally gives more accurate reproduction of the EDF energy as a function of deformation.

The strength of the quadrupole interaction  $\chi$  is determined by fitting the cost of deforming. Thus we fix the quadrupole-quadrupole strength  $\chi$  in the following manner: (i) for several values of the deformation parameter  $\beta_2$  we compute the energy  $E^{HF}(\beta_2)$  obtained with the functional within a Skyrme HF calculation with constraints on the quadrupole moment; (ii)  $\chi$  is then fitted such that the HF energies obtained with the effective Hamiltonian  $\hat{H}$  (1), reproduces  $E^{HF}(\beta_2)$ . As seen in Fig. 1 the cost of deforming can be reproduced in a reasonable way. The approximation of only having a single quadrupole term limits the range of deformations that can be described. Thus the agreement is expected to deteriorate for larger deformations where more complex shapes become important.

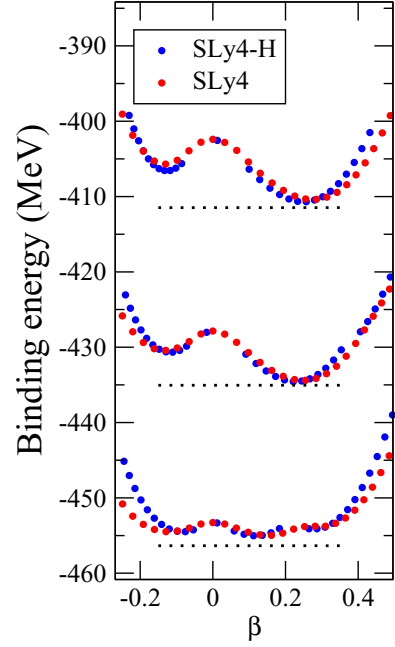


FIG. 1. HF energy versus deformation  $\beta$  for  $^{48,50,52}\text{Cr}$  using a basis of 12 spherical oscillator shells ( $N_{\text{max}} = 11$ ). Experimental binding energies are shown with dashed lines. The SLy4 EDF results are obtained with the code [25] and the results abbreviated SLy4-H are obtained with the effective Hamiltonian (1).

For the pairing part of the Hamiltonian  $H_p$  [Eq. (4)] the interaction strength is determined applying the uniform model of Ref. [19]. This treatment of pairing is similar to the one in the Cranked-Nilsson-Strutinsky-Bogoliubov model (CNSB) [26]. First we assume the empirical estimate of the average gap,  $\tilde{\Delta}_0 = 0.7 \times 12 / \sqrt{A}$  [27]. The reduction factor of 0.7 comes from compensating for the effect of particle-number projection [28,29]. Then, the strength  $G_q(\tilde{\Delta}_0)$  is found by solving the uniform model [19]. For each nucleus we obtain different strengths  $G_q$  by solving separately for protons and neutrons,

$$(\tilde{\Delta}_0 - G_q) = 2S e^{-\frac{1}{G_q \rho}}, \quad (12)$$

where the pairing window is set to  $S = 30$  MeV in the spherical basis. Here  $\rho$  denotes the level density averaged in the energy window taken from the spherical HF solution. Note that the left-hand side is modified to take into account the contribution of the exchange term in the pairing. The full treatment of the exchange term is needed to avoid the singularities when applying the projection operator and gives an extra contribution when breaking a pair (see Appendix of Ref. [26]).

In the way described in this section, all the coupling constants of the effective Hamiltonian becomes determined from the underlying reference functional. In this paper we consistently apply the SLy4 parametrization of the Skyrme interaction [30] as a reference functional and denote the resulting Hamiltonian SLy4-H.

### C. Collective coordinates

In the previous sections, we defined the effective Hamiltonian and its parameters. In the following, we define the many-body basis within which the Hamiltonian is solved. Our basis states consist of HFB vacua obtained with the effective Hamiltonian for several values of the deformation located on a grid. This grid is constructed by solving the HFB equations for the Hamiltonian in Eq. (1) with constraints on

$$\beta_x = \frac{4\pi}{5} \frac{\langle \hat{Q}_{20} \rangle}{\langle r^2 \rangle}, \quad (13)$$

$$\beta_y = \frac{4\pi}{5} \sqrt{2} \frac{\langle \hat{Q}_{22} + \hat{Q}_{2-2} \rangle}{\langle r^2 \rangle}, \quad (14)$$

with  $\langle \bullet \rangle$  the expectation value of the operator respect to the deformed HFB states and  $\hat{Q}_{2\mu} = r^2 Y_{2\mu}$ . From this, one obtains the familiar  $\beta = \sqrt{\beta_x^2 + \beta_y^2}$ , which defines the degree of quadrupole deformation, and  $\gamma = \arctan(\frac{\beta_y}{\beta_x})$ , which defines the triaxiality. We also use the cranking method with a constraint on

$$j_x = \langle \hat{J}_x \rangle. \quad (15)$$

In addition, we also include a variation of the pairing strengths  $G_p(\tilde{\Delta}_0)$  and  $G_n(\tilde{\Delta}_0)$  by scaling the pairing gaps  $\tilde{\Delta}_0 = g_q \Delta_0$ . The many-body basis states are obtained as the lowest-energy solutions to the HFB equations in a grid of  $\beta$ ,  $\gamma$ ,  $j_x$ ,  $g_p$ , and  $g_n$  values. The grids are generated by sampling a region of the  $(\beta, \gamma)$  plane. Each point of the plane can be associated with a certain value of  $(j_x, g_p, g_n)$ . We have allowed a few different values of each of these variables and randomly assigned one of these values for each  $(\beta, \gamma)$  point. Only HFB states below a certain cutoff energy are kept and accepted as basis states.

This choice of generating coordinates attempts to account for the most important collective degrees of freedom namely: collective vibrations in the quadrupole degrees of freedom, rotations, and pairing correlations. In order to improve the accuracy for a larger class of states in the spectrum one would need to enlarge the basis further by, for instance, including states built through quasiparticle (QP) excitations. Another way of introducing such noncollective particle-type excitations is to act on the basis states with an excitation operator:

$$\begin{aligned} |\phi_1\rangle &= \mathcal{N} e^{\hat{Z}} |\phi_0\rangle \\ &= \mathcal{N} (1 + \hat{Z} + \frac{1}{2} \hat{Z}^2 + \dots) |\phi_0\rangle, \end{aligned} \quad (16)$$

where  $\mathcal{N}$  is a normalization constant and  $\hat{Z}$  is a two-quasiparticle creation operator:

$$\hat{Z} = \sum_{k < k'} z_{k,k'} \beta_k^\dagger \beta_{k'}^\dagger. \quad (17)$$

The  $z_{k,k'}$  elements are chosen as

$$z_{k,k'} = e^{-(E_k + E_{k'}) / (k_B T)} \times p, \quad \text{for } k' > k, \quad (18)$$

with  $z_{k,k'} = -z_{k',k}$ , for  $k' < k$  to make  $z$  skew symmetric. This ensures that the new state  $|\phi_1\rangle$  can be expressed as a single HFB determinant [31]. For each many-body state and for each matrix element,  $p$  is randomly taken as  $\pm 1$ . The value of  $k_B T$

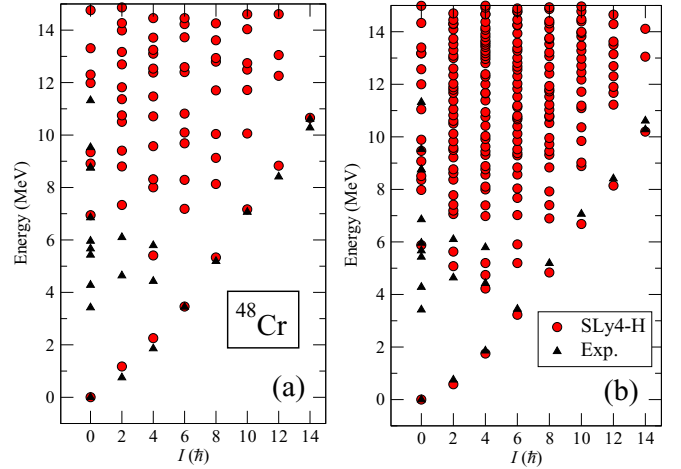


FIG. 2. Calculated positive parity and even spin spectra for  $^{48}\text{Cr}$ , (a) without temperature excitations and in (b) with inclusion of single-particle type excitations using the temperature method (16) with  $b = 0.45$ . In both panels we used the SLy4-H Hamiltonian with 11 oscillator shells ( $N_{\text{max}} = 10$ ) for the single-particle basis and a grid consisting of  $N_\phi = 191$  HFB vacua for the many-body basis. Experimental data taken from Ref. [32]. The Hamiltonian for each spin has been diagonalized using the number of natural states found from the Hill-Wheeler equation (28) considering the yrast state.

is obtained from a parameter  $b$  as,

$$k_B T = -(E_1 + E_2) / \ln(b). \quad (19)$$

The smallest value of the sum of the lowest QP energies;  $E_1 + E_2$  for either protons or neutrons are used for both particle species in this relation.

The operator acts separately on neutron and proton parts of the states with the result that the lowest two-quasiparticle excitations are added to the states with weights determined by the parameter  $b$ . Multi-quasiparticle excitations will also be added due to the structure of the series but with diminishing weights. The random sign ensures that even if the energy surface is oversampled the states will still have orthogonal components allowing for the extraction of more independent solutions. The quasiparticles are taken to have preserved parity and signature ( $r_x \phi = e^{-i\pi \hat{J}_x} \phi$ ) quantum numbers. The quasiparticle pairs in Eq. (17) are restricted to belong to the group with positive parity and signature  $(\pi, r_x) = (1, 1)$  so that when acting on an HFB state, the generated excitations do not change the symmetry of the state. That is, the matrix elements  $z_{k,k'}$  can be characterized by the quantum numbers of the quasiparticle pairs and these are restricted to have positive signature and parity and to be of the same nucleon species. After acting on one of the basis states, the new state obtained contains a mixture of multi-quasiparticle excitations with random signs that reduces overcompleteness of the basis. In this way, this temperature-inspired method introduces particle-type excitations into the basis in order to complement the more collective excitations introduced through the generating coordinates.

An example is shown in Fig. 2. As seen from this figure the application of the excitation operator allows for a much

larger number of eigenstates to be found and an improved convergence of the yrast band.

#### D. Efficient symmetry restoration

After generating the many-body basis, the following step consists in computing the matrix elements for the projected overlap and Hamilton operator. By construction, the HFB vacua do not have either a good number of nucleons or angular momentum. As a consequence, it is necessary to introduce projection operators to restore symmetries and evaluate states with definite values for quantum numbers. The matrix elements read,

$$\begin{aligned} O_{IK,JK'} &= \langle \phi_I | \hat{P}_{MK}^{I\dagger} \hat{P}_{MK'}^I \hat{P}_Z \hat{P}_N | \phi_J \rangle \\ &= \langle \phi_I | \hat{P}_{KK'}^I \hat{P}_Z \hat{P}_N | \phi_J \rangle \\ &= \sum_i w_i \langle \phi_I | \hat{R}_i | \phi_J \rangle \end{aligned} \quad (20)$$

$$\begin{aligned} H_{IK,JK'} &= \langle \phi_I | \hat{P}_{MK}^{I\dagger} \hat{H} \hat{P}_{MK'}^I \hat{P}_Z \hat{P}_N | \phi_J \rangle \\ &= \langle \phi_I | \hat{H} \hat{P}_{KK'}^I \hat{P}_Z \hat{P}_N | \phi_J \rangle \\ &= \sum_i w_i \langle \phi_I | \hat{H} \hat{R}_i | \phi_J \rangle, \end{aligned} \quad (22)$$

where  $\hat{P}$  are projection operators for neutron, proton number, and angular momentum.  $\hat{R}_i = \hat{R}(\alpha_i, \beta_i, \gamma_i, \theta_i^Z, \theta_i^N)$  are the rotations over the gauge and Euler angles, with the corresponding weights  $w_i$  (see, e.g., Refs. [33,34]). From each HFB state one can often project out several many-body states with different  $K$  projections. The final energies are invariant with respect to the orientation in the laboratory frame, so these matrix elements do not depend on the  $M$  quantum number.

The computation of the matrix elements above is time consuming due to the projection operators, which involve angular integrations over angles in space and gauge space. As a consequence, it is essential to be able to perform accurate and systematic truncations in the computations of these matrix elements. Our truncation scheme is based on the Bloch-Messiah decomposition, which allows us to rewrite the Bogoliubov matrices  $U$  and  $V$  as  $U = D\bar{U}C$ ,  $V = D^*\bar{V}C$  where  $D$  and  $C$  are both unitary matrices and  $D$  defines the so-called canonical basis associated with the Bogoliubov vacuum [31].  $\bar{U}$  and  $\bar{V}$  can be chosen as diagonal and skew symmetric, respectively. The matrix  $\bar{V}$  is written in terms of blocks of dimension  $2 \times 2$  with elements  $(v_i, -v_i)$  where  $v_i^2$  is the occupation probability of the canonical basis state  $i$  (the matrix elements  $u_i$  of  $\bar{U}$  are such that  $u_i^2 + v_i^2 = 1$ ). Our truncation criteria is defined by first sorting the  $N$  occupation numbers  $v_i^2$  in descending order (see Ref. [16]) and then truncating the canonical basis, that is we consider a smaller size  $n \leq N$  where  $n$  is such that

$$\sum_i v_i^2 - \sum_i^n v_i^2 < 0.01. \quad (23)$$

The occupation numbers differ for each state so each state is thus truncated differently and stored in the smaller representation before calculation of the matrix elements. The truncated states thus define our new basis states where long tails and numerical noise have been removed. Using these

truncated states, the overlaps of rotated Bogoliubov states are computed and all the calculations are reduced to the minimal occupied subspace using the Bloch-Messiah transformation (see Refs. [16,31,35] and Appendix A).

An unpaired HFB vacua will have a dimension  $n$  corresponding to the number of particles and exact zeros outside of this space. Paired vacua will have varying dimension depending on the pairing distribution. It is thus essential to be able to calculate overlaps of states having very different sizes. While the applied overlap formula allows the calculations of overlaps when states have  $v_i$ s exactly equal to zero it also allows us to reduce the dimension by keeping only nonzero  $v_i$ s thus keeping only the essential information and therefore greatly reducing the computational time [16].

#### E. Odd numbers of nucleons

The computation for nuclei with an odd number of nucleons proceeds similarly to the even-even case. In this paper, we consider the case of even-odd nuclei. Having generated the set of HFB vacua as described in the previous section, the odd-state basis is generated as a set of one quasiparticle creation operators acting on the HFB states, namely:

$$|\Phi^{\text{odd}}\rangle \equiv \beta_a^\dagger |\Phi^{\text{even}}\rangle. \quad (24)$$

The corresponding Bogoliubov matrices  $U^{\text{odd}}$  and  $V^{\text{odd}}$  are easily obtained by replacing the  $a$ th column in  $U$  and  $V$  by the corresponding column in  $V^*$ ,  $U^*$  [31]. Obviously, as in the case of even nuclei, the ability to truncate in a systematic manner is also critical for an efficient computation in the odd case. In this context, the computation of the overlap for odd system is performed using the truncated formula in Ref. [16]. The application of the Bloch-Messiah decomposition allows us to rewrite the odd vacua as a product of three matrices

$$U^{\text{odd}} = D^{\text{odd}} \bar{U}^{\text{odd}} C^{\text{odd}}, \quad (25)$$

$$V^{\text{odd}} = D^{\text{odd}*} \bar{V}^{\text{odd}} C^{\text{odd}}, \quad (26)$$

where  $D^{\text{odd}}$  and  $C^{\text{odd}}$  are unitary matrices and,

$$\begin{aligned} \bar{U}^{\text{odd}} &= \begin{pmatrix} 0 & 0 & 0 & 0 & 0 \\ 0 & 1 & 0 & 0 & 0 \\ 0 & 0 & u_2 & 0 & 0 \\ 0 & 0 & 0 & u_2 & 0 \\ 0 & 0 & 0 & 0 & \ddots \end{pmatrix}, \\ \bar{V}^{\text{odd}} &= \begin{pmatrix} 1 & 0 & 0 & 0 & 0 \\ 0 & 0 & 0 & 0 & 0 \\ 0 & 0 & 0 & v_2 & 0 \\ 0 & 0 & -v_2 & 0 & 0 \\ 0 & 0 & 0 & 0 & \ddots \end{pmatrix}. \end{aligned} \quad (27)$$

The structure of  $U^{\text{odd}}$  and  $V^{\text{odd}}$  is almost identical to the even-even case except for the odd particle, which is unpaired. This unpaired particle is, by convention, placed in the first position in both matrices. The truncations of matrices can then proceed similarly as in the even case. That is, the truncation is dictated by the values  $v_i$  of the paired particles. After decomposing the matrices in this form the calculation of projected Hamiltonian

matrix elements proceeds similarly as in the even case (see Appendix A).

### F. Hill-Wheeler equation

The spectra are obtained by solving the Hill-Wheeler (HW) equation [31]. The state solutions of the HW equations are, by construction, eigenstates of the parity and angular momentum operators  $I^2$  and  $I_z$ .

In matrix form the Hill-Wheeler equation reads,

$$Hh = EOh, \quad (28)$$

with  $H$  from Eq. (22),  $O$  from Eq. (20), and where  $h$  and  $E$  are the resulting eigenvector and eigenvalue solutions. This equation can be solved separately for each total angular momentum  $I$  giving energies  $E_n^I$  and corresponding eigenstates as expansions in terms of the projected HFB states:

$$|IM, n\rangle = \sum_{a=1}^{N_a} \sum_{K=-I}^I h_{aK,n}^I \hat{P}_{MK}^I \hat{P}^N \hat{P}^Z |\phi_a\rangle. \quad (29)$$

In this equation,  $|\phi_a\rangle$  are the  $N_a$  HFB basis states and the operators  $\hat{P}$  are projection operators for proton number, neutron number, and angular momentum. The coefficients  $h_{aK,n}^I$  are found from the Hill-Wheeler equation in the basis of projected HFB states and scaled such that  $|IM, n\rangle$  becomes normalized.

### G. Transitions and quadrupole moments

Because angular momentum projection is performed, the model gives eigenstates in the laboratory system as output. This makes it natural and straightforward to calculate observables avoiding the process of extracting them from the internal system, which inevitably contains approximations. Furthermore, since the model allows for calculations in large model spaces there is no need for effective charges.

#### 1. Reduced transition probability

Because of the interaction between the charged nucleus and the electromagnetic field, it is possible to have transitions between eigenstates of the nuclear Hamiltonian by emitting (or absorbing) a photon. Those transitions can be classified into electromagnetic multipoles. For a given multipole of order  $\lambda$  the emitted (absorbed) photon will carry a total angular momentum of  $\lambda\hbar$ .

The transition rate  $T$  (the lifetime is given by  $\tau = \hbar/T$ ) from an initial to a final nuclear eigenstate for an electrical multipole is given by Ref. [31], in SI units

$$T_{fi}^{\lambda\mu} = \frac{2}{\varepsilon_0 \hbar} \frac{\lambda + 1}{\lambda [(2\lambda + 1)!!]^2} \left( \frac{E_\gamma}{\hbar c} \right)^{2\lambda+1} |\langle \Psi_f | \hat{Q}_{\lambda\mu} | \Psi_i \rangle|^2, \quad (30)$$

where  $E_\gamma$  is the energy of the emitted photon. This expression is derived from Fermi's golden rule up to first order in perturbation theory.

Due to the fact that quadrupole deformations are the dominant shape degrees of freedom for atomic nuclei, the quadrupole mode is the most prominent one for the radiation. Hence, here we will consider  $E2$  transitions.

A nuclear eigenstate has definite values for the total angular momentum  $I$  and its projection  $M$ . Often one does not want to distinguish between different  $M$  values; neither for final nor initial states. Therefore one averages over initial  $M$  (assuming an equal distribution of initial  $M$  values) and sum over final  $M$  (the final  $M$  value is not important). This type of rate is therefore given by (for  $\lambda = 2$ )

$$\begin{aligned} T_{fi}^{\lambda=2} &= \frac{1}{2I_i + 1} \sum_{M_f M_i \mu} T_{fi}^{2\mu} \\ &= \frac{1}{75\varepsilon_0 \hbar} \left( \frac{E_\gamma}{\hbar c} \right)^5 \frac{1}{2I_i + 1} \sum_{M_f M_i \mu} |\langle I_f M_f | \hat{Q}_{2\mu} | I_i M_i \rangle|^2 \\ &\equiv \frac{1}{75\varepsilon_0 \hbar} \left( \frac{E_\gamma}{\hbar c} \right)^5 B(E2; I_i \rightarrow I_f), \end{aligned} \quad (31)$$

where the reduced transition probability  $B$  has been defined. The  $B(E2)$  values do not contain the large  $\gamma$ -ray energy dependence of the transition rate. Therefore, calculations of the reduced transition probability are more easily compared to experiment than the transition rate.

#### 2. Projection and GCM

In the model presented in this paper, projections onto good particle number and angular momentum are performed. In this approach, the  $n$ th state for given  $I$  and  $M$  can be written as in Eq. (29).

With those states, the matrix element for the reduced transition probability becomes,

$$\begin{aligned} \langle I' M', n' | \hat{Q}_{2\mu} | IM, n \rangle &= \\ &= \sum_{a', a=1}^{N_a} \sum_{K'=-I'}^{I'} \sum_{K=-I}^I h_{a'K',n'}^{I'*} h_{aK,n}^I \\ &\quad \times \langle \phi_{a'} | \hat{P}_{M'K'}^{I'\dagger} \hat{Q}_{2\mu} \hat{P}_{MK}^I \hat{P}^N \hat{P}^Z | \phi_a \rangle, \end{aligned} \quad (32)$$

where it has been used that  $\hat{Q}_{2\mu}$  conserves particle number. In Ref. [33] it is stated that

$$\hat{P}_{M'K'}^{I'\dagger} \hat{Q}_{2\mu} \hat{P}_{MK}^I = C_{IM2\mu}^{I'M'} \sum_{\nu} C_{I,K'-\nu,2\nu}^{I'K'} \hat{Q}_{2\nu} \hat{P}_{K'-\nu,K}^I, \quad (33)$$

where the  $C$ 's are Clebsch-Gordan coefficients with notation such that the two angular momenta in the subscript couple to the angular momenta in the superscript. Hence, in total we get

$$\begin{aligned} \langle I' M', n' | \hat{Q}_{2\mu} | IM, n \rangle &= C_{IM2\mu}^{I'M'} \sum_{a', a=1}^{N_a} \sum_{K'=-I'}^{I'} \sum_{K=-I}^I h_{a'K',n'}^{I'*} h_{aK,n}^I \\ &\quad \times \sum_{\nu} C_{I,K'-\nu,2\nu}^{I'K'} \\ &\quad \times \langle \phi_{a'} | \hat{Q}_{2\nu} \hat{P}_{K'-\nu,K}^I \hat{P}^N \hat{P}^Z | \phi_a \rangle. \end{aligned} \quad (34)$$

In the expression for the  $B(E2)$  value, Eq. (31), the summations over  $M', M$ , and  $\mu$  only involves the first Clebsch-Gordan coefficient in the above matrix element. Using orthogonally relations for the Clebsch-Gordan coeffi-

cients, the sum reduces to

$$\sum_{M'M\mu} |C_{IM2\mu}^{I'M'}|^2 = \sum_{M'} 1 = 2I' + 1. \quad (35)$$

The final expression for the reduced transition probability is then

$$B(E2; I \rightarrow I') = \frac{2I' + 1}{2I + 1} \left| \sum_{a', a=1}^{N_a} \sum_{K'=-I'}^{I'} \sum_{K=-I}^I h_{a'K',n}^{I'*} h_{aK,n}^I \times \sum_{\nu} C_{I,K'-\nu,2\nu}^{I'K'} \langle \phi_{a'} | \hat{Q}_{2\nu} \hat{P}_{K'-\nu,K}^I \hat{P}^N \hat{P}^Z | \phi_a \rangle \right|^2. \quad (36)$$

In the cases where measurements exist, we also compare the spectroscopic quadrupole moment, defined as:

$$Q_{\text{spec}} = \sqrt{\frac{16\pi}{5}} \langle IM = I | \hat{Q}_{20} | IM = I \rangle. \quad (37)$$

This  $Q_{\text{spec}}$  is defined in the laboratory frame and becomes identically zero for  $I < 1$ .

### III. RESULTS

To test the developed model, calculations have been performed for five nuclei: four even-even nuclei, the three chromium isotopes  $^{48,50,52}\text{Cr}$ ,  $^{24}\text{Mg}$ , and the even-odd  $^{49}\text{Cr}$ . The formalism of extracting the  $B(E2)$  transitions and the quadrupole moment has been implemented only for even-even nuclei. The results are compared both with experiment and with other theoretical calculations. The chromium isotopes have been chosen in order to test the model when going from the deformed  $^{48}\text{Cr}$  to the more spherical  $^{52}\text{Cr}$ .

The experimental values for energies and transitions are taken from Ref. [32] if not otherwise stated. Experimental values for the spectroscopic quadrupole moments are rare but the few found are from Ref. [36]. Some of the transition rates have not been explicitly given in Ref. [32], but are instead extracted from  $\gamma$  energies and lifetimes according to Eq. (31). In the case where the state decays in several channels, the lifetime for channel  $a$ ,  $\tau_a$ , can be calculated from the  $\gamma$  intensity,  $I(\gamma)$ , with the expression

$$\tau_a = \tau \frac{\sum_i I_i(\gamma)}{I_a(\gamma)}, \quad (38)$$

where the sum goes over all channels.

#### A. Generation of collective subspace for the different nuclei

The points in the grid are defined by starting at spherical shape. For each new point the  $\gamma$  angle is increased with the golden angle  $\theta \simeq 137.508$ . The radial distance  $\beta$  is increased with the square root of the number of points. This generates a rather homogeneously sampled circular area in the  $(\beta, \gamma)$  plane. With cranking included, the surface will have mirror symmetry in the  $y$  axis. An example for  $^{48}\text{Cr}$  with  $j_x = 0$  is shown in Fig. 3. As seen from this figure  $^{48}\text{Cr}$  has a prolate minimum centered around  $\gamma = 0^\circ$  with  $\beta \sim 0.25$ .

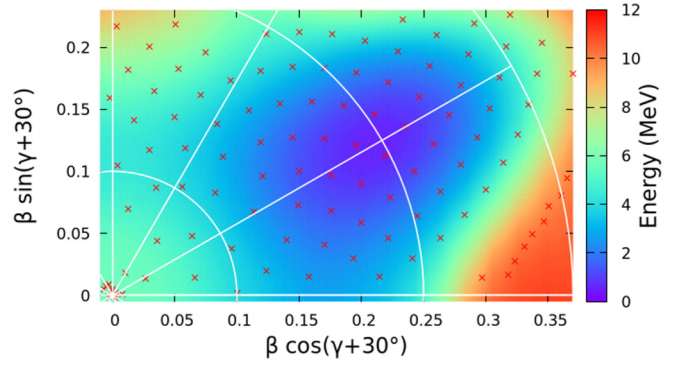


FIG. 3. HFB energy versus deformation for  $^{48}\text{Cr}$  with the SLy4-H Hamiltonian. Twelve oscillator shells are used for the single-particle basis ( $N_{\text{max}} = 11$ ),  $j_x = 0$  and the pairing interaction strength is kept fixed ( $g_p, g_n$ ) = (1, 1). The  $(\beta, \gamma)$  plane is drawn with the standard Lund convention with  $\gamma = 60^\circ$  along the positive  $y$  axis.

As  $j_x$  is increased this minimum will move towards  $\gamma = 60^\circ$  where the rotation eventually becomes noncollective since the shape is then rotationally symmetric around the cranking axis ( $x$  axis).

For the pairing we use a grid in two variables  $g_p$  and  $g_n$ . These grids are constrained to four values: {0.6, 1.0, 1.4, 1.8}. These values specify scaling of the pairing  $\Delta$  values. A value of 1.0 would imply generating the surface with only the self-consistent pairing. While a value of 1.4 implies generating basis states with a stronger interaction that gives 1.4 times larger pairing gaps.

For the cranking frequency  $\omega$  we choose a grid of three different  $j_x$  values {0, 4, 8} and the  $\omega$  values needed for each state to obtain those  $j_x$  values are estimated as  $\omega = \frac{1}{2\mathcal{J}(\beta, \gamma, \Delta)} (2j_x + 1)$  [19]. The moment of inertia is estimated as in Ref. [37], where for simplicity we used  $\Delta = 0.1$  MeV for all points. For each point in the  $(\beta, \gamma)$  plane values of  $g_p, g_n$  and  $j_x$  are randomly drawn from the allowed sets in order to create states that sample the relevant many-body space. For the even-even nuclei we have used basis states with signature  $r_x = 1$  and for the odd  $^{49}\text{Cr}$  we compare the use of both  $r_x = \pm i$ .

In the numerical calculation of the excitation operator [Eq. (16)] we have used  $b = 0.45$  [see Eq. (19)]. This implies that for the particle species that is easiest to excite the lowest two-quasiparticle excitation within the considered symmetry group is added to the state with a weight of 0.45. See Appendix B for a discussion over how this specific value for  $b$  has been selected.

For all even-even chromium isotopes, the same calculation parameters have been used (values for  $^{49}\text{Cr}$  and  $^{24}\text{Mg}$  are given below). That is, 12 major shells in the harmonic oscillator basis generated by an updated version of the code HOSPHE [38]. The  $(\beta, \gamma)$  plane has been sampled with 300 states within  $\beta \leq 0.5$  and  $-30^\circ \leq \gamma \leq 150^\circ$ . Since we are interested in the low-energy part of the spectra it is sufficient to consider basis states up to a given cutoff. Therefore only states within 12 MeV from the state with the lowest calculated energy has been kept, which is sufficient to cover the energy range of the experimental yrast states. This resulted

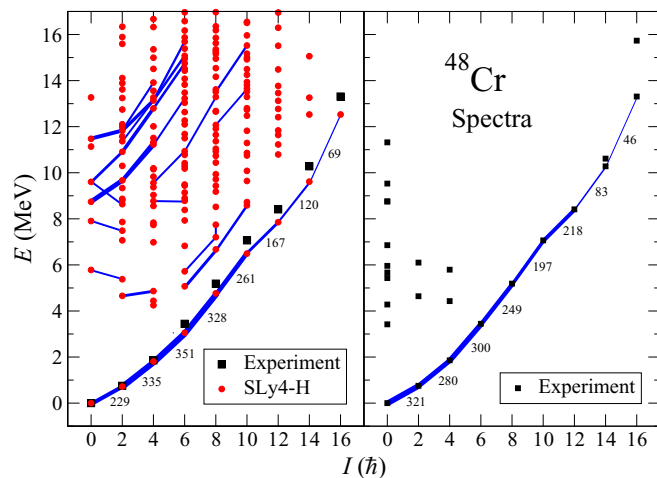


FIG. 4. Positive parity and even spin spectra including  $B(E2)$  transitions for  $^{48}\text{Cr}$ . Theory to the left and experiment to the right. The experimental values for the yrast band are also shown together with theory for easier comparison. The strengths for the transitions are indicated by the thickness of the lines and are explicitly given in  $\text{e}^2\text{fm}^4$  for the yrast band.

in basis sizes of 198, 217, and 206 for the  $^{48}\text{Cr}$ ,  $^{50}\text{Cr}$ , and  $^{52}\text{Cr}$  isotopes, respectively. For the numerical computation of the projections, 10 points have been used in the number projections for both types of nucleons and (9, 18, 36) points in the  $(\alpha, \beta, \gamma)$  angles for the angular momentum projection. These number of points for the angular momentum projection are obtained after applying symmetries to reduce the integration interval and corresponds to (36, 36, 36) points in the full space, see, e.g., Refs. [33,34].

The  $B(E2)$  values are calculated for every transition that differ with two or zero units of spin. However, with few exceptions discussed, only transitions over 10 W.u are plotted in the spectra.

### B. $^{48}\text{Cr}$

The spectra for  $^{48}_{24}\text{Cr}_{24}$ , both the calculated and the experimental values, together with the strongest transitions, are shown in Fig. 4. The calculation shows the characteristic of a rotor,  $E_{\text{rot}} \propto I(I+1)$ , for the yrast band up to spin  $10\hbar$  where the first back bending happens.

The general behavior of a deformed and rotating nucleus approaching a terminating states has been discussed in Ref. [39]. For a low angular momentum the rotation is of a collective nature with the rotation axis perpendicular to the symmetry axis of the nucleus. With increasing angular momentum the valence nucleons tend to align their spins with the rotation axis. This continues until all valence nucleons are fully aligned with the rotation axis. Then no further angular momentum can be built and one has reached the terminating state. In that state the rotation axis is parallel with the symmetry axis and therefore the rotation is of a single-particle nature.

In  $^{48}\text{Cr}$ , the termination is expected to happen at  $I = 16$ . This can be understood from the fact that  $^{48}\text{Cr}$  has four protons

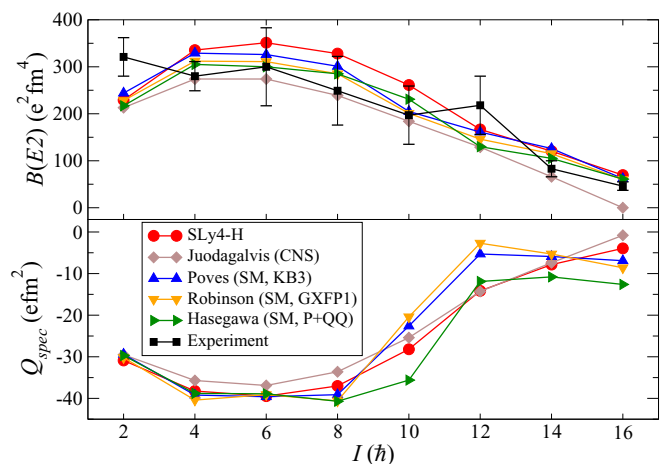


FIG. 5.  $B(E2)$  transitions ( $I \rightarrow I-2$ ) and spectroscopic quadrupole moments for the yrast band in  $^{48}\text{Cr}$ . No experimental data has been found for  $Q_{\text{spec}}$ .

and four neutrons in the  $f_{7/2}$  subshell. Aligning all valence nucleons within this subshell results in spin  $16\hbar$ .

The evolution of the internal structure of  $^{48}\text{Cr}$  with angular momentum up to its terminating state has been investigated in Ref. [40] within the cranked Nilsson-Strutinsky (CNS) model. The conclusion in that paper is that the intrinsic deformation goes from axially symmetric prolate over triaxial shapes to end up in a slightly oblate shape when the terminating state is reached.

Comparisons of transitions and quadrupole moments between results from our model and results obtained from CNS is shown in Fig. 5. Also three shell-model (SM) calculations for three different interactions in the full  $fp$  space are included [41–43].

The results from our Hamiltonian, denoted SLy4-H, are in agreement with the previous CNS and SM calculations. Both the  $B(E2)$  and the  $Q_{\text{spec}}$  curves resembles the ones for a rigid rotor up spin  $6\hbar$ . For higher angular momentum, the  $B(E2)$  values are approaching zero; showing that the states are indeed of a single-particle nature rather than a mixed collective one. There is also a good agreement for the prediction of the properties of the spectroscopic quadrupole moment (37). All the models predict a quite drastic change in the shape associated with the back bend at  $I = 10 - 12$  and that the nucleus becomes close to spherical at the terminating state.

In a  $N = Z$  nucleus, as for  $^{48}\text{Cr}$ , it is expected that neutron-proton pairing should play an important role. This is because both the protons and the neutrons occupy the same valence space. Thus, they have maximal spatial overlap, cf. Ref. [44] for a discussion of neutron-proton pairing, the different types from the different isospin channels and their possible effects. Even though our model does not include neutron-proton pairing, it is interesting to compare the back bending from the calculations with experiment.

It can be seen in Fig. 6 that the back bending in SLy4-H occurs at the same spin and have the same magnitude as in experiment. However, the  $\gamma$  energies are consistently lower for all angular momenta (except at the back bending). This is



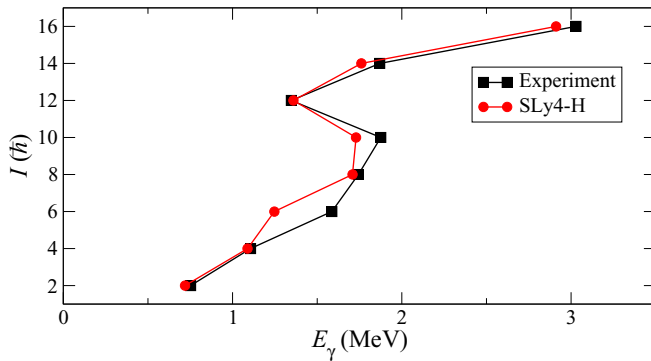


FIG. 6. Released  $\gamma$ -ray energies for transitions  $I + 2 \rightarrow I$  for the yrast band of  $^{48}\text{Cr}$ . The back bending at  $I = 10\hbar$  indicates a change in the internal structure.

in line with Refs. [41,45]. In both those papers they separate out the neutron-proton pairing in the isospin  $T = 0$  channel from the rest of the pairing to see its effect. They both find that, without this pairing, the spectra becomes suppressed. This would imply a shift to the left for the back-bending curve in Fig. 6 with around 0.2–0.5 MeV.

### C. $^{49}\text{Cr}$

We now focus on the even-odd  $^{49}\text{Cr}_{25}$  isotope. Shell-model calculations in the  $pf$  shell have shown a good reproduction of the ground-state (GS) band and its rotational patterns at low spin can be described by the particle-rotor model as a  $K^\pi = 5/2^-$  band based on the  $\nu [312]5/2^-$  Nilsson orbital [46].

Figure 7 shows the computed energies of states in the GS band of  $^{49}\text{Cr}$  in several bases. The results in Fig. 7(a) are obtained, without cranking, in a basis of 116 states whereas for the results in Figs. 7(b), 7(c) the cranking is included and the number of basis states is 114 and 156, respectively. Without cranking, the states in the odd basis with opposite

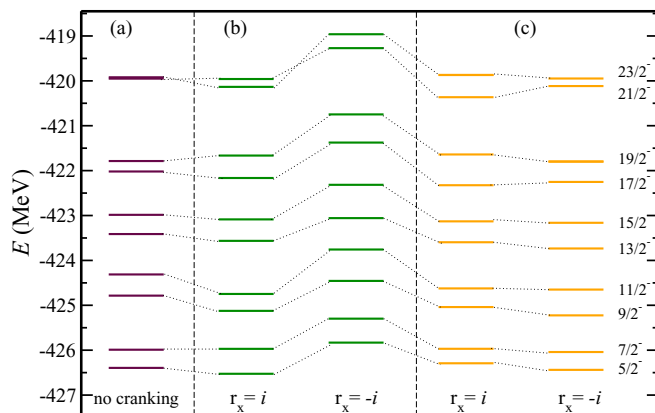


FIG. 7. Energies of the GS rotational band in  $^{49}\text{Cr}$  computed in different bases. In (a) the basis includes 116 states and the cranking is switched off. In (b) and (c), respectively, 114 and 156 states are included in the basis and the cranking is switched on. Results on the left (right) side of (b) and (c) are obtained in a basis with signature  $r_x = i$  ( $-i$ ).

signature are related by time reversal and consequently the computed energies are identical whether the basis states have a signature  $r_x = i$  or  $r_x = -i$ . This is not the case anymore when the cranking is included and we show in Figs. 7(b), 7(c) results for both signatures. All parameters are the same as for  $^{48}\text{Cr}$  and for each calculation, the basis is formed by blocking the QP [see Eq. (24)] with the lowest energy.<sup>1</sup>

A general property is that states with  $I = 1/2, 5/2, 9/2 \dots$  are best described within a basis with signature  $r_x = -i$  and states with  $I = 3/2, 7/2, 11/2 \dots$  are best described within a basis with  $r_x = i$  [47]. However, from Fig. 7 one notices that the difference in the energies computed with the different signatures diminishes when the basis increases. It is then more natural to consider as the most precise energy for a state of angular momentum  $I$ , the lowest energy among the two energies computed in the largest basis with  $r_x = i$  and  $r_x = -i$ . As one can see in Fig. 7, the difference in the GS energy obtained with  $r_x = i$  and  $r_x = -i$  is  $\sim 700$  keV for the basis made of 114 states [Fig. 7(b)] and decreases to less than 150 keV in the larger basis [Fig. 7(c)]. It is also worth noting that the difference between the lowest computed GS energies with cranking [Figs. 7(b) and 7(c)] and the GS energy without cranking [Fig. 7(a)] is  $\sim 100$  keV.

Taking the lowest state in the bigger basis we obtain a binding energy  $B^{th} = -426.395$  MeV [that is, the energy of the GS  $I^\pi = 5/2^-$  in Fig. 7(c) in the basis with  $r_x = -i$ ], which is slightly lower than the experimental binding energy  $B^{exp} = -422.051$  MeV. In order to gain some insights into the amount of correlations included beyond the mean field, it is instructive to compare  $B^{th}$  with the lowest mean-field energy among the basis states. For each odd state  $|\Phi^{a,i}\rangle \equiv \beta_a^\dagger |\Phi_i\rangle$ , we can assign a mean-field energy  $E_0^{(a,i)} = E_0^i + e_a$ , with  $E_0^i$  the HFB energy of the even-even vacuum  $|\Phi_i\rangle$  and  $e_a$  the energy of the QP  $a$ . In that particular case, the lowest mean-field energy among the basis states is  $-420.560$  MeV, which implies that the beyond mean-field effects included in the theory, lower the energy by  $\approx 5.8$  MeV.

We show in Fig. 8, a comparison between the computed excitation energies and the experimental data. As one can see, the data are well reproduced by the calculation. In particular, our calculations reproduce the occurrence of a back bending for spin  $19/2\hbar$ . The GS rotational band splits into two branches corresponding to sequences of states  $\Delta I = 2$ . As one can see in Fig. 8 at low spin, the two branches are close to each other and start to diverge for larger  $I$ .

### D. $^{50}\text{Cr}$

The spectrum for  $^{50}\text{Cr}_{26}$  is given in Fig. 9. We calculated up to spin  $14\hbar$ , which is expected to be the terminating spin of the ground-state configuration.

<sup>1</sup>Due to the application of the excitation operator (16) on the HFB vacua, the QPs are no longer eigenstates for a finite value of  $kT$ . Nevertheless, the QP with the lowest energy computed before the application of the operator (16), is selected to construct the odd state basis. This is justified by the fact that for low  $kT$  value, the ordering of the average QP energy is not dramatically affected.

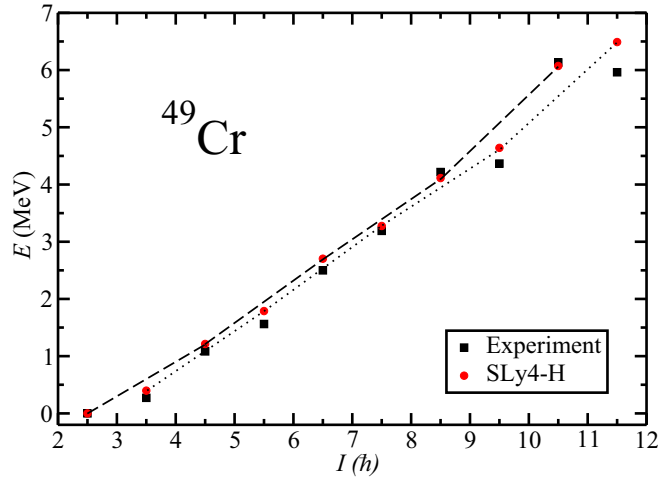


FIG. 8. Excitation energies of states in the GS rotational band in  $^{49}\text{Cr}$ . The black squares denote experimental data, whereas the red circles show the results of the computation in the largest basis considered (156 states) with cranking. For each  $I$  the computed energies corresponds to the lowest energies among the spectra displayed in Fig. 7(c). The dash and dotted lines denotes the two branches, which connect the calculated states with  $\Delta I = 2$  (see text).

The calculations reproduce the two lowest  $10^+$  states that are very close in energy and that are also seen in experiment. In fact, the calculations suggest that the ground-state band, which starts from the first  $0^+$  state, continues up to  $I = 14$  via the  $10_2^+$  state. The yrast states for  $I = 10, 12$ , and  $14$  seem to originate from a different band. This is further confirmed from the spectroscopic quadrupole moments in Fig. 10. At  $I = 10$  they change sign, indicating a change in the internal structure.

Experiments also show a stronger  $B(E2)$  transition from the  $10_2^+$  state than from the  $10_1^+$  state. Unfortunately, there are no data of transition strengths for higher spin states above the yrast band.

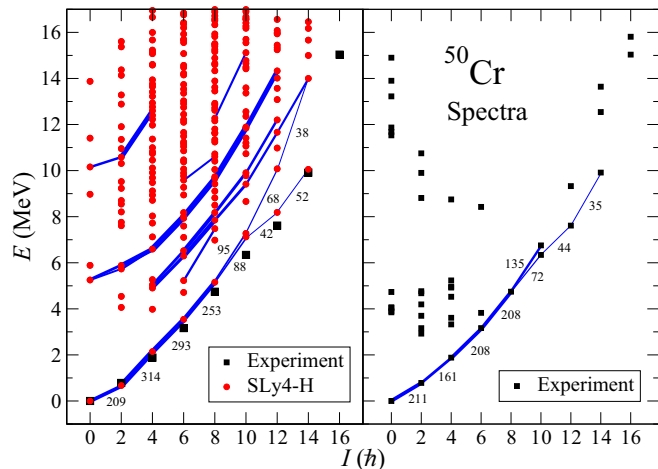


FIG. 9. Same as Fig. 4 for the spectra and  $B(E2)$  transitions in  $^{50}\text{Cr}$ .

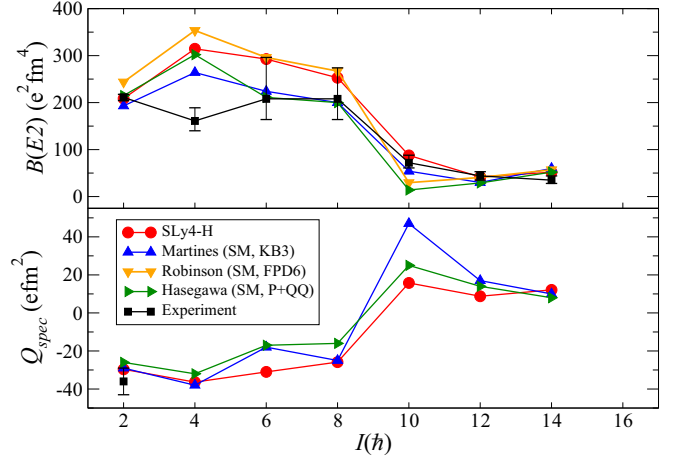


FIG. 10.  $B(E2)$  transitions and spectroscopic quadrupole moments for the yrast band in  $^{50}\text{Cr}$ .

For the purpose of this paper, CNS calculations for  $^{50}\text{Cr}$  have been performed. The results from those calculations can be used to interpret the internal structure of the states. It was found that the  $10_2^+$  state indeed gets its angular momentum from collective rotation; in the same way as the lower part of the yrast band does. Whereas the  $10_1^+$  state is predicted to be prolate with the symmetry axis parallel to the rotational axis. This implies that the rotation is built up by single-particles spins.

Furthermore, the CNS calculations predict two more bands with positive parity. One band is located around 2.2 MeV above the yrast band and is built upon a  $1p - 1h$  excitation of the neutrons. This band is in fact divided into two nearly degenerated bands with opposite signature. Another excited band is found around 3.7 MeV above the yrast band and is built upon a  $2p - 2h$  neutron excitation.

As seen in Fig. 9, our model produce the same band structure as the CNS calculations. Hence, for this nucleus, the two methods are consistent with each other. In experiments no excited bands with positive parity and even spins have yet been identified.

In Fig. 10 our results for the transitions and spectroscopic quadrupole moments are compared with experiment and shell-model calculations for three different interactions [43,45,48]. It is interesting to note the discrepancy between experiment and all of the shown theoretical calculations for the  $B(E2; 4 \rightarrow 2)$  value. Also, the experimental value is not what one would expect from a rotational model. In fact, the transitions for  $^{48}\text{Cr}$  also do not follow a rotor description for low angular momenta. But for that nucleus it is the  $B(E2; 2 \rightarrow 0)$  value that is high. So, for both  $^{48}\text{Cr}$  and  $^{50}\text{Cr}$  the ratio  $B(E2; 4 \rightarrow 2)/B(E2; 2 \rightarrow 0)$  is less than 1. This in contrast of the rotational model where the ratio is 1.43, which is in more agreement with the calculations. This discrepancy has been pointed out before [49]. In Ref. [50] it is suggested the that unusual ratio can be understood in a collective picture with the inclusion of appropriate three-body forces. This is shown explicitly for  $^{170}\text{Os}$  in the interacting boson model.

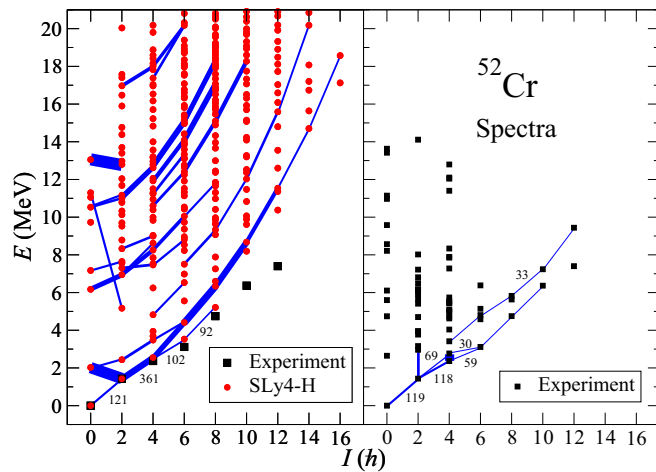


FIG. 11. Same as Fig. 4 for the spectra and  $B(E2)$  transitions in  $^{52}\text{Cr}$ . The two identified experimental bands are indicated with thin lines when there are no measured  $B(E2)$  values.

### E. $^{52}\text{Cr}$

In  $^{52}\text{Cr}_{28}$  the eight valence neutrons fill up the  $f_{7/2}$  orbit and therefore the nucleus is expected to be less deformed and close to a spherical shape. And, indeed, both experiment and our calculations show a spectra in which the yrast band is more similar to a linear vibrational one than to a quadratic rotational one, see Fig. 11.

The calculated energies for the yrast band fits well with experiment up to the expected termination at  $I = 8\hbar$ . In contrast, the model does not agree with experiment for the yrast states with larger angular momenta; too high energies are obtained. However, the angular momenta, which are assigned to those states from experiment, are considered uncertain. Our calculations support the possibility that these states have a different angular momenta than the ones they have been attributed.

In experiment, two rotational bands with positive parity and even spins have been identified. The ground-state band up to spin  $10\hbar$  and a second band built from the  $4_3^+$  state, which goes up to spin  $12\hbar$ . And as seen from the transitions in Fig. 11, our model indeed predicts a rotational band just above the yrast band. The calculated second band starts at the  $0_2^+$  state and passes over the  $2_2^+$  and  $4_2^+$  states. For  $I \leq 6\hbar$  the calculated transitions between the bands are strong. This indicates a similar internal structure of the two bands for low angular momenta.

Those two bands, the shell closure yrast band and the excited rotational band have been investigated by *Caurier et al.* [51]. They found that the yrast band indeed is composed mainly by the closed-shell configuration. In contrast, the excited rotational band is built upon the  $0_2^+$  state with an internal structure dominated by two neutrons above the  $f_{7/2}$  orbital. In addition, they calculate  $Q_{\text{spec}}$  and  $B(E2)$  values for the excited band, which are compared in Fig. 12 with our results. Also, in Fig. 12, the results for the yrast band is compared with a SM calculation [52]. While there is a good overall agreement between theory and experiment our

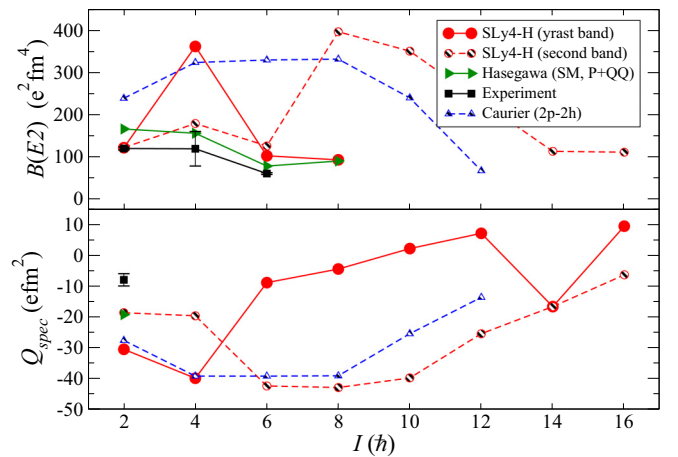


FIG. 12. Transitions and quadrupole moments for  $^{52}\text{Cr}$ . The dashed lines are for the second band.

calculations predict the bands slightly closer in energy and more mixed than in experiment for  $I = 0 - 4$ .

### F. $^{24}\text{Mg}$

The main reason to test the model on the nucleus  $^{24}\text{Mg}_{12}$  is to compare the results with the ones presented in Refs. [53] and [54]. In those references they use a similar procedure as the one given in this paper. That is, a mean-field basis of HFB states with different constraints on the  $\beta\gamma$  deformations, projections onto good quantum numbers, and mixing using the GCM.

The main difference is that those works use the same interaction throughout the whole calculation; SLy4 in Ref. [53] and Gogny D1S in Ref. [54]. Since those forces are density dependent it is not well defined how to perform the mixing of states. Therefore, the density is replaced with the transition density to overcome this problem. It has been pointed out that this procedure can lead to poles in the energy for some deformations [15]. This issue is absent in our model since we postulate a Hamiltonian, which can be used in a straightforward way in the mixing. Our results, together with experiment, are shown in Fig. 13 and in Fig. 14  $B(E2)$  values and quadrupole moments are compared both with experiments and the previous calculations.

The parameters of the calculation for  $^{24}\text{Mg}$  are the same as for the chromium isotopes except for the following: 10 major shells in the harmonic oscillator single-particle basis, 300 states to sample the  $\beta\gamma$  plane within  $\beta \leq 0.8$  and  $-30^\circ \leq \gamma \leq 150^\circ$ . Keeping states below 25 MeV in excitation energy resulted in 133 basis states. The number of points for the projections are 10 for the particle numbers of both types of nucleons and (6, 12, 24) for the  $(\alpha, \beta, \gamma)$  angles of the angular momentum [corresponding to (24, 24, 24) points in the full space]. The cutoff value for the displayed  $B(E2)$  transitions is 7 W.u.

For the spectra, the Gogny force succeeds to reproduce experimental values in an excellent way, at least up to  $I = 6$ . To the advantage of our model is that it reproduces the yrast  $8_1^+$

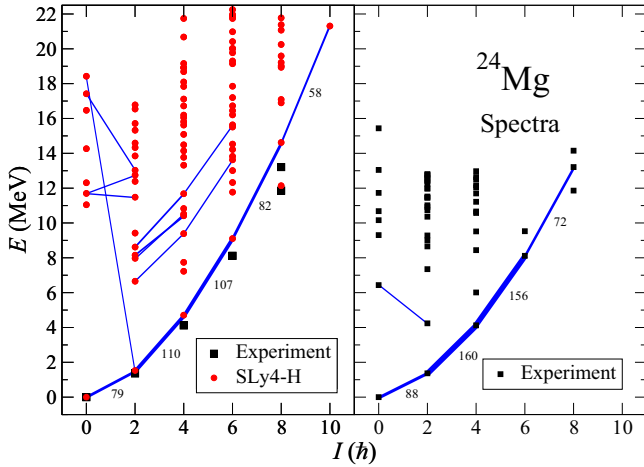


FIG. 13. Same as Fig. 4 for spectra and transitions in  $^{24}\text{Mg}$ . The experimental values for the  $I = 8$  states, both energies and the transitions, are taken from Ref. [55].

state below the rotational band, which is seen in experiment. This state is not reported in Ref. [54].

The  $8_1^+$  state has also been reproduced in SM calculations and in the CNS method; both presented in Ref. [56]. In that paper, using the CNS method, it is found that this state is maximally aligned with its symmetry axis parallel to the axis of rotation. Hence, it is predicted to be a noncollective state. Indeed, this is expected to happen at  $I = 8$ , which is the maximal spin that can be produced for the four valence particles confined to the orbits of  $d_{5/2}$  character. In contrast, the  $8_2^+$  state, which belongs to the ground-state band, is of a collective nature with the axis of rotation perpendicular to the symmetry axis. This ground-state band continues until it terminates at  $I = 12$  [56]. Note the similarity with  $^{50}\text{Cr}$  where the aligned state is yrast for  $I = 10$ , while the ground band terminates for  $I = 14$ .

Also for the transitions the results from Refs. [53] and [54] fit well with experiment. Again at least up to  $I = 6$ . But the trend that the  $B(E2)$  values increase with higher spin

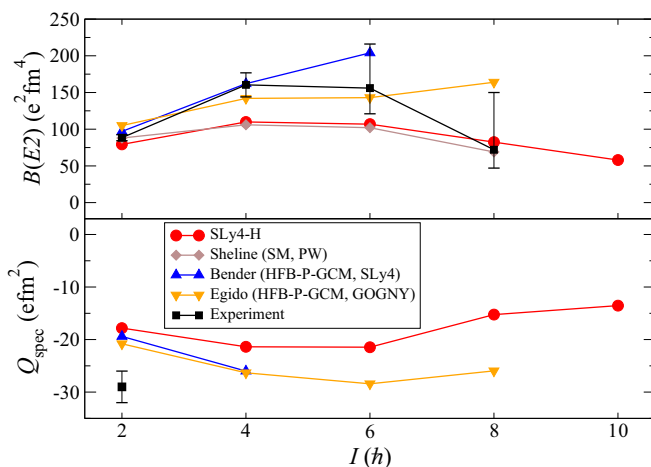


FIG. 14. Transitions and quadrupole moments for  $^{24}\text{Mg}$ .

seems questionable. It is not what one would expect; neither from experiment nor from experience for rotational bands approaching a terminating state. Our model agrees more with shell-model calculations and have the expected decrease with spin.

#### IV. CONCLUSIONS

The method introduced works surprisingly well for the description of both spectra and transitions. Both transitions and delicate structure information such as back bending are correctly reproduced for all nuclei considered. Defining a Hamilton operator allows the many-body calculations to be carried out in a straightforward manner, without any need for additional assumptions to treat the density-dependent parts of the functional. In this work, the postulated separable Hamiltonian is constrained to reproduce the energy surface of a reference EDF. Correctly describing the detailed landscapes of energy minima and corresponding shapes is one of the basic components needed in order to reproduce the experimental spectra. We have chosen the effective Hamiltonian as simple as possible, while still capable of producing realistic results. The simplicity of the interaction, together with the reduction to the smallest space using the Bloch-Messiah method, allows for advanced many-body calculations. We have incorporated both collective and single-particle-type excitations using around 200 HFB vacua in the basis. The number of points needed in the angular momentum projection increases rapidly when considering higher angular momentum states [57] and in this work the calculations have been carried out to spin 16 while maintaining the refined many-body mixing of the states. This allowed us to cover the spin range up to the terminating states seen in these nuclei. Thus, to obtain in the complete space a fully symmetry restored description of the gradual transition from collective rotation to the noncollective terminating states based on the GCM.

The present results give encouraging prospects for the future. Any nuclear interaction can be expressed in terms of sums of separable terms, through, e.g., a singular value decomposition or more refined physically motivated expansions [58,59]. Thus, the simple expansion explored here can be fully developed into a converging expansion. The question in this respect is the applicability and efficiency of the method. The present study demonstrates the numerical efficiency of the approach. The effective Hamilton operator employed here may still be extended with more terms while keeping the calculations feasible. The first such terms to consider could be an improved pairing part, hexadecapole terms in the particle-hole part, and a refined treatment of Coulomb.

#### ACKNOWLEDGMENTS

B.G.C. and J.L. thank the Knut and Alice Wallenberg Foundation (KAW 2015.0021) for financial support. J.R. thanks the Crafoord foundation for support. A.I. was supported by Swedish Research Council 2020-03721. We also acknowledge the Lunarc computing facility.

**APPENDIX A: COMPUTATION OF MATRIX ELEMENTS**

The Hamiltonian matrix elements in Eq. (22) can be expressed [31],

$$\langle a|\hat{H}|b\rangle = \langle a|b\rangle \frac{1}{2} [\text{Tr}(\rho\Gamma) - \text{Tr}(\Delta\kappa_{01}^*)]. \quad (\text{A1})$$

The contribution of the two-body interaction in Eq. (1) to the particle-hole fields  $\Gamma$  becomes

$$\begin{aligned} \Gamma_{ij} = & -\chi \sum_{\mu} \tilde{Q}_{ij}^{2\mu} \text{Tr}(\rho(\tilde{Q}^{2\mu})^T) + \chi \sum_{\mu} [\tilde{Q}^{2\mu} \rho (\tilde{Q}^{2\mu})^T]_{ij} \\ & + G_{ij} [P\rho^T P]_{ij} \end{aligned} \quad (\text{A2})$$

and the contribution to the particle-particle fields  $\Delta$  becomes

$$\Delta_{ij} = \frac{1}{2} P_{ij} \sum_k G_{ik} [\kappa_{10} P]_{kk} - \chi \sum_{\mu} [\tilde{Q}^{2\mu} \kappa_{10} \tilde{Q}^{2\mu}]_{ij}. \quad (\text{A3})$$

In order to speed up the calculations it is important to reduce the dimensions to the minimal occupied subspace [35,60]. We choose a block size that is the maximum value of  $n_a$  and  $n_b$  [see Eq. (23)] to denote the size of the top left block in the equations below. The BM transformation is used to transform the  $(U, V)$  matrices of the vacua. As an example for the  $|b\rangle$  vacua we obtain  $U_b = D_b \bar{U}_b C_b$  and  $V_b = D_b^* \bar{V}_b C_b$  with

$$\bar{V}_b = \begin{pmatrix} v_b & 0 \\ 0 & 0 \end{pmatrix} \text{ and } \bar{U}_b = \begin{pmatrix} u_b & 0 \\ 0 & \mathbb{1} \end{pmatrix}.$$

The transitional densities  $\rho$ ,  $\kappa_{10}$ , and  $\kappa_{01}^*$  [31] can then be transformed and expressed:

$$D_b^\dagger \rho D_a = \bar{\rho} = \begin{pmatrix} \bar{\rho}_{11} & 0 \\ 0 & 0 \end{pmatrix} \quad (\text{A4})$$

$$D_b^\dagger \kappa_{10} D_a^* = \bar{\kappa}_{10} = \begin{pmatrix} (\bar{\kappa}_{10})_{11} & (\bar{\kappa}_{10})_{12} \\ 0 & 0 \end{pmatrix} \quad (\text{A5})$$

$$D_b^T \kappa_{01}^* D_a = \bar{\kappa}_{01}^* = \begin{pmatrix} (\bar{\kappa}_{01}^*)_{11} & 0 \\ (\bar{\kappa}_{01}^*)_{21} & 0 \end{pmatrix} \quad (\text{A6})$$

with

$$\bar{\rho}_{11} = v_b^* U^{-1} v_a^T \quad (\text{A7})$$

$$(\bar{\kappa}_{10})_{11} = v_b^* U^{-1} u_a^T \quad (\text{A8})$$

$$(\bar{\kappa}_{10})_{12} = (\kappa_{10})_{11} d_{11}^{-1} d_{12} \quad (\text{A9})$$

$$(\bar{\kappa}_{01}^*)_{11} = -u_b^* U^{-1} v_a^T \quad (\text{A10})$$

$$(\bar{\kappa}_{01}^*)_{21} = d_{21} d_{11}^{-1} (\bar{\kappa}_{01}^*)_{11}, \quad (\text{A11})$$

where

$$U^{-1} = (v_a^T d_{11}^T v_b^* + u_a^T d_{11}^{-1} u_b^*)^{-1} \quad (\text{A12})$$

and

$$D_b^T D_a^* = \begin{pmatrix} d_{11} & d_{12} \\ d_{21} & d_{22} \end{pmatrix}. \quad (\text{A13})$$

For the blocks of the transformed interaction we introduce the notation:

$$\bar{Q}^{2\mu} = (D_a^\dagger \tilde{Q}^{2\mu} D_b)_{11} \quad (\text{A14})$$

$$\bar{P}_1 = (D_a^\dagger P D_a^*)_{11} \quad (\text{A15})$$

$$\bar{P}_2 = (D_b^\dagger P D_b^*)_{11} \quad (\text{A16})$$

$$\bar{P}_{11} = (D_a^\dagger P D_b^*)_{11} \quad (\text{A17})$$

$$\bar{P}_{12} = (D_a^\dagger P D_b^*)_{12} \quad (\text{A18})$$

$$\bar{P}_{21} = (D_a^\dagger P D_b^*)_{21}. \quad (\text{A19})$$

If we furthermore decompose the all matrices into proton and neutron parts and use  $q$  to label the proton or neutron blocks we obtain the full expression for the matrix elements in the optimal space and with proton and neutron parts explicitly written out as:

$$\begin{aligned} \langle a|\hat{H}_Q + \hat{H}_P|b\rangle = & -\langle a|b\rangle \frac{\chi}{2} \sum_{\mu q q'} (-1)^\mu \text{Tr}(\bar{\rho}_{11}^q \bar{Q}^{2\mu, q}) \times \text{Tr}(\bar{\rho}_{11}^{q'} \bar{Q}^{2(-\mu), q'}) + \langle a|b\rangle \frac{\chi}{2} \sum_{q\mu} (-1)^\mu \text{Tr}(\bar{\rho}_{11}^q \bar{Q}^{2\mu, q} \bar{\rho}_{11}^{q'} \bar{Q}^{2(-\mu), q}) \\ & + \langle a|b\rangle \frac{1}{2} \sum_q G_q \text{Tr}(\bar{\rho}_{11}^q \bar{P}_{q,1} (\bar{\rho}_{11}^q)^T \bar{P}_{q,2}^*) - \langle a|b\rangle \frac{1}{4} \sum_q G_q \text{Tr} \left( [(\bar{\kappa}_{10}^q)_{11}, (\bar{\kappa}_{10}^q)_{12}] \begin{bmatrix} \bar{P}_{q,11}^* \\ \bar{P}_{q,21}^* \end{bmatrix} \right) \\ & \times \text{Tr} \left( [\bar{P}_{q,11}, \bar{P}_{q,12}] \begin{bmatrix} (\bar{\kappa}_{01}^{*q})_{11} \\ (\bar{\kappa}_{01}^{*q})_{21} \end{bmatrix} \right) + \langle a|b\rangle \frac{\chi}{2} \sum_{\mu q} \text{Tr} \left( \bar{Q}^{2\mu, q} [(\bar{\kappa}_{10}^q)_{11}, (\bar{\kappa}_{10}^q)_{12}] (D_a^\dagger \tilde{Q}^{2\mu, q} D_b)^* \begin{bmatrix} (\bar{\kappa}_{01}^{*q})_{11} \\ (\bar{\kappa}_{01}^{*q})_{21} \end{bmatrix} \right), \end{aligned} \quad (\text{A20})$$

where in addition we have used the symmetries of our interaction:

$$\begin{aligned} Q_{kl}^{2\mu*} &= Q_{kl}^{2\mu} \\ Q_{kl}^{2\mu} &= (-1)^\mu Q_{lk}^{2-\mu} \\ P_{kl} &= -P_{lk} \\ P_{kl}^* &= P_{kl}. \end{aligned}$$

In the code, this expression is further optimized by moving as many operations as possible outside the loops of gauge and Euler angles. The effect of symmetry restoration does not change the canonical occupation numbers but only leads to a matrix multiplication acting on the  $D_b$  matrix. Expression (A20) becomes the same for HFB states with odd number parity, the only modification being the application of the Bloch-Messiah decomposition for odd states as described in Sec. II E.

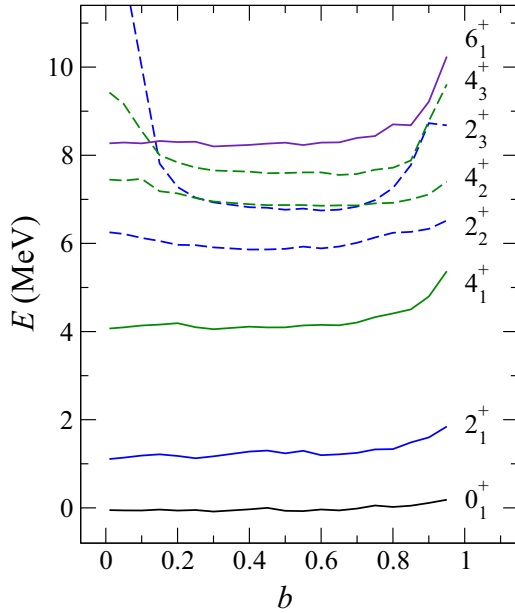


FIG. 15. Calculated low-energy spectra for  $^{24}\text{Mg}$  as a function of the parameter  $b$  (19). The energies  $E$  are relative to the ground-state energy for  $b = 0.45$ . The states shown in the plot are the yrast states (filled lines) and the first two excited states (dashed lines) that have excitation energy below 9 MeV. The used values for  $b$  are distributed between 0.01 and 0.95.

## APPENDIX B: HOW THE TEMPERATURE AFFECTS THE SPECTRA

In this Appendix, we investigate how different amount of temperature in the excitation operator (16) affects the spectra. In particular, we want to find an appropriate value for the

parameter  $b$  (19) to be used in our calculations. This parameter determines the weights of the multiquasiparticle states that are added to each HFB vacua in the many-body basis.

In order to find an optimal value for  $b$  we perform a series of calculations for  $^{24}\text{Mg}$  using different values of  $b$ . These calculations use ten oscillator shells in the single-particle basis, the  $(\beta, \gamma)$  plane is sampled with 119 HFB vacua within  $\beta \leq 0.8$  and  $-30 \text{ deg} \leq \gamma \leq 150 \text{ deg}$ . The nucleus  $^{24}\text{Mg}$  is further investigated in Sec. III F.

In the temperature method each HFB vacua is promoted to a superposition of multiquasiparticle states through the excitation operator. According to Thouless' theorem [31], and because the matrix  $z$  (16) is chosen to be skew symmetric, the superposition is ensured to be a HFB state. The 119 promoted HFB states are then used as a new many-body basis in the framework of GCM, together with symmetry restoration, in order to obtain the nuclear spectra.

In restoring the symmetries, we use 10 points over the gauge angle for the particle number projection for both types of nucleons; and (6, 12, 24) points over the Euler angles  $(\alpha, \beta, \gamma)$  for the angular momentum projection.

In Fig. 15 it is shown how the energies, for some of the lowest-energy states in  $^{24}\text{Mg}$ , are affected by the temperature. For the yrast band the energies are rather constant up to  $b = 0.7$ . They fluctuate within approximately  $\pm 0.1$  MeV. This is in agreement with the interpretation that the yrast band is of a collective nature. Hence, the quasiparticle excitations do not improve the HFB-basis for those states.

However, as seen in Fig. 15, the first and second excited states are more dependent on the temperature. Indeed, those states are expected to involve quasiparticle excitations on top of the yrast states. The excited states have an improved convergence in the range  $b = [0.3, 0.6]$ . Therefore, we have chosen the value in the middle:  $b = 0.45$ .

- 
- [1] T. Skyrme, *Nucl. Phys.* **9**, 615 (1958).  
[2] B. G. Carlsson, J. Dobaczewski, and M. Kortelainen, *Phys. Rev. C* **78**, 044326 (2008).  
[3] F. Raimondi, B. G. Carlsson, and J. Dobaczewski, *Phys. Rev. C* **83**, 054311 (2011).  
[4] W. Ryssens and M. Bender, *Phys. Rev. C* **104**, 044308 (2021).  
[5] M. Bender, P.-H. Heenen, and P.-G. Reinhard, *Rev. Mod. Phys.* **75**, 121 (2003).  
[6] G. Scamps, S. Goriely, E. Olsen, M. Bender, and W. Ryssens, *Eur. Phys. J. A* **57**, 333 (2021).  
[7] P. Veselý, J. Toivanen, B. G. Carlsson, J. Dobaczewski, N. Michel, and A. Pastore, *Phys. Rev. C* **86**, 024303 (2012).  
[8] B. G. Carlsson, J. Toivanen, and A. Pastore, *Phys. Rev. C* **86**, 014307 (2012).  
[9] B. G. Carlsson and I. Ragnarsson, *Phys. Rev. C* **74**, 044310 (2006).  
[10] J. P. Delaroche, M. Girod, J. Libert, H. Goutte, S. Hilaire, S. Péru, N. Pillet, and G. F. Bertsch, *Phys. Rev. C* **81**, 014303 (2010).  
[11] K. Nomura, R. Rodríguez-Guzmán, and L. M. Robledo, *Phys. Rev. C* **101**, 014306 (2020).  
[12] Y. Alhassid, G. F. Bertsch, L. Fang, and B. Sabbey, *Phys. Rev. C* **74**, 034301 (2006).  
[13] B. G. Carlsson, J. Toivanen, and U. von Barth, *Phys. Rev. C* **87**, 054303 (2013).  
[14] F. Dönau, *Phys. Rev. C* **58**, 872 (1998).  
[15] M. Bender, T. Duguet, and D. Lacroix, *Phys. Rev. C* **79**, 044319 (2009).  
[16] B. G. Carlsson and J. Rotureau, *Phys. Rev. Lett.* **126**, 172501 (2021).  
[17] A. Sámár-Roth, D. M. Cox, D. Rudolph, L. G. Sarmiento, B. G. Carlsson, J. L. Egido, P. Golubev, J. Heery, A. Yakushev, S. Åberg *et al.*, *Phys. Rev. Lett.* **126**, 032503 (2021).  
[18] K. Kumar and B. Sørensen, *Nucl. Phys. A* **146**, 1 (1970).  
[19] S. Nilsson and I. Ragnarsson, *Shapes and Shells in Nuclear Structure* (Cambridge University Press, Cambridge, 1995).  
[20] A. Idini, F. Barranco, and E. Vigezzi, *Phys. Rev. C* **85**, 014331 (2012).  
[21] G. Potel, A. Idini, F. Barranco, E. Vigezzi, and R. A. Broglia, *Phys. Rev. C* **96**, 034606 (2017).  
[22] G. P. Aguilar and R. A. Broglia, *The Nuclear Cooper Pair: Structure and Reactions* (Cambridge University Press, Cambridge, 2021).

- [23] N. Tsunoda, T. Otsuka, K. Takayanagi, N. Shimizu, T. Suzuki, Y. Utsuno, S. Yoshida, and H. Ueno, *Nature (London)* **587**, 66 (2020).
- [24] J. Dudek, Z. Szymański, T. Werner, A. Faessler, and C. Lima, *Phys. Rev. C* **26**, 1712 (1982).
- [25] R. N. Perez, N. Schunck, R.-D. Lasserri, C. Zhang, and J. Sarich, *Comput. Phys. Commun.* **220**, 363 (2017).
- [26] B. G. Carlsson, I. Ragnarsson, R. Bengtsson, E. O. Lieder, R. M. Lieder, and A. A. Pasternak, *Phys. Rev. C* **78**, 034316 (2008).
- [27] A. Bohr and B. Mottelson, *Nuclear Structure: Vol. 1, Single-Particle Motion* (World Scientific, Singapore, 1998).
- [28] H. Olofsson, R. Bengtsson, and P. Möller, *Nucl. Phys. A* **784**, 104 (2007).
- [29] A. Idini, G. Potel, F. Barranco, E. Vigezzi, and R. A. Broglia, *Phys. Rev. C* **92**, 031304(R) (2015).
- [30] E. Chabanat, P. Bonche, P. Haensel, J. Meyer, and R. Schaeffer, *Nucl. Phys. A* **635**, 231 (1998).
- [31] P. Ring and P. Schuck, *The Nuclear Many-Body Problem* (Springer-Verlag, New York, 1980).
- [32] Evaluated nuclear structure data file, 2021, <http://www.nndc.bnl.gov>.
- [33] K. Enami, K. Tanabe, and N. Yoshinaga, *Phys. Rev. C* **59**, 135 (1999).
- [34] B. Bally and M. Bender, *Phys. Rev. C* **103**, 024315 (2021).
- [35] J. M. Yao, J. Meng, P. Ring, and D. Pena Arteaga, *Phys. Rev. C* **79**, 044312 (2009).
- [36] N. J. Stone, *At. Data Nucl. Data Tables* **111-112**, 1 (2016).
- [37] R. Bengtsson and S. Åberg, *Phys. Lett. B* **172**, 277 (1986).
- [38] B. Carlsson, J. Dobaczewski, J. Toivanen, and P. Vesely, *Comput. Phys. Commun.* **181**, 1641 (2010).
- [39] A. Afanasjev, D. Fossan, G. Lane, and I. Ragnarsson, *Phys. Rep.* **322**, 1 (1999).
- [40] A. Juodagalvis, I. Ragnarsson, and S. Åberg, *Phys. Lett. B* **477**, 66 (2000).
- [41] A. Poves, *J. Phys. G: Nucl. Part. Phys.* **25**, 589 (1999).
- [42] S. J. Q. Robinson, T. Hoang, L. Zamick, A. Escuderos, and Y. Y. Sharon, *Phys. Rev. C* **89**, 014316 (2014).
- [43] M. Hasegawa, K. Kaneko, and S. Tazaki, *Nucl. Phys. A* **674**, 411 (2000).
- [44] A. L. Goodman, *Phys. Rev. C* **60**, 014311 (1999).
- [45] S. J. Q. Robinson, A. Escuderos, and L. Zamick, *Phys. Rev. C* **72**, 034314 (2005).
- [46] G. Martínez-Pinedo, A. P. Zuker, A. Poves, and E. Caurier, *Phys. Rev. C* **55**, 187 (1997).
- [47] A. Bohr, B. Mottelson, *Nuclear Structure: Vol. 2, Nuclear Deformations* (World Scientific, Singapore, 1969).
- [48] G. Martínez-Pinedo, A. Poves, L. M. Robledo, E. Caurier, F. Nowacki, J. Retamosa, and A. Zuker, *Phys. Rev. C* **54**, R2150 (1996).
- [49] D. Hertz-Kintish, L. Zamick, and S. J. Q. Robinson, *Phys. Rev. C* **90**, 034307 (2014).
- [50] T. Wang, *Europhys. Lett.* **129**, 52001 (2020).
- [51] E. Caurier, F. Nowacki, and A. Poves, *Nucl. Phys. A* **742**, 14 (2004).
- [52] M. Hasegawa, K. Kaneko, and S. Tazaki, *Prog. Theor. Phys.* **107**, 731 (2002).
- [53] M. Bender and P.-H. Heenen, *Phys. Rev. C* **78**, 024309 (2008).
- [54] T. R. Rodríguez and J. L. Egido, *Phys. Rev. C* **81**, 064323 (2010).
- [55] L. Fifield, M. Hurst, T. Symons, F. Watt, C. Zimmerman, and K. Allen, *Nucl. Phys. A* **309**, 77 (1978).
- [56] R. K. Sheline, I. Ragnarsson, S. Aberg, and A. Watts, *J. Phys. G* **14**, 1201 (1988).
- [57] C. W. Johnson and K. D. O'Mara, *Phys. Rev. C* **96**, 064304 (2017).
- [58] A. Tichai, R. Schutski, G. E. Scuseria, and T. Duguet, *Phys. Rev. C* **99**, 034320 (2019).
- [59] V. O. Nesterenko, J. Kvasil, and P.-G. Reinhard, *Phys. Rev. C* **66**, 044307 (2002).
- [60] P. Bonche, J. Dobaczewski, H. Flocard, P.-H. Heenen, and J. Meyer, *Nucl. Phys. A* **510**, 466 (1990).